

A NUMERICAL INVESTIGATION OF IMPINGING JETS

N.S. Barlow¹, B.T. Helenbrook² and S.P. Lin³

¹Corresponding Author, natesbarlow@hotmail.com

²Primary Advisor, helenbrk@clarkson.edu

³Research Advisor, gw02@clarkson.edu

ABSTRACT Steady, incompressible flow solutions are found numerically for a radially expanding liquid sheet in order to confirm analytical results for inviscid flow and to investigate viscous and nonlinear effects. An hp-finite element method is used to perform the numerical simulations. Comparisons are made to theoretical predictions of the radius where the sheet becomes unstable. To determine the critical radius, the inlet Weber number is slowly reduced until the critical radius is within the simulated domain. This causes the sheet to change from a symmetric shape to an asymmetric stable shape. Simulations are run for sheets with liquid Reynolds numbers of 25, 50, 100, and 200, liquid-to-gas density ratios of 32, 160, and 800, and liquid-to-gas viscosity ratios of 12.5, 25, and 50. These parameters have little effect on the critical sheet radius; It always remains near the point at which the Weber number based on the sheet thickness is one, confirming the theoretical work of G.I. Taylor. We also perform unsteady simulations with forced sinusoidal pulses at the sheet inlet. We observe that the pulses cause two different speed waves to travel downstream for Weber numbers greater than one. We also witness wave deceleration for Weber numbers less than one, confirming the predictions of inviscid linear stability analysis.

Keywords: Impinging Jets, Liquid Sheet, Weber Number, Finite Element Method, Bifurcation

1. INTRODUCTION

The control of the onset of liquid sheet breakup is of interest in such applications as nuclear safety, spray combustion, agricultural sprays, ink jet printing, fiber and sheet drawing, powdered milk processing, powder metallurgy, toxic material removal, and the encapsulation of biomedical materials. Liquid sheets can be formed in a number of ways. One of which is by two perfectly opposed impinging liquid jets, as shown in Figure 1. This phenomenon was first studied by Savart (1833), who showed that the sheet thickness depends on the distance away from the axis of impingement [1]. Experiments were later done by Bond (1935) for water sheets, with a strong emphasis on the effect of surface tension [2]. Taylor (1959) investigated perturbed waves on the sheet's free surface and confirmed that the sheet breaks up at a critical radius determined by the Weber number of the sheet [3]. The critical radius of breakup was explored further by Huang (1970) and break-up regimes were established [4]. Variations of this case have since been looked into for different impingement angles [5, 6, 7, 8, 9]. The propagating surface waves have been investigated by Lin (2003) through a rigorous stability analysis and a relationship was found between the wave speed and the Weber number [10, 11].

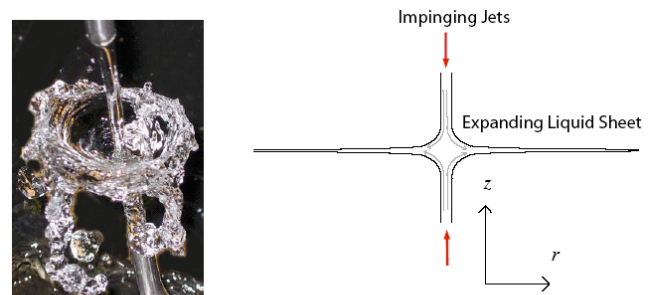


Figure 1. Two jets impinging to form a liquid sheet.

The goal of this paper is provide a numerical model for a liquid sheet which can be compared to the theoretical and experimental work mentioned above. We begin with a description of the physical configuration and a review of the analytic results pertaining to this configuration. A formulation of our corresponding mathematical model and a description of the numerical method and the boundary conditions is given. Next, we examine the steady state results, in which the Weber number at sheet asymmetry is determined for different densities, viscosities, and Reynolds numbers. The remaining sections examine the unsteady behavior of the sheet when a pulse is introduced at the inlet.

2. PHYSICAL PROBLEM

The The configuration is shown in Figure 1 where the r and z are the radial and axial cylindrical coordinates. The problem is assumed to be axisymmetric about the z -axis. The two liquid jets are assumed incompressible and

immiscible with the surrounding gas. Gravitational forces are neglected. Typically, analyses focus on the region where the sheet becomes thin and linearized results can be obtained. This region is defined by $H/r \ll 1$ where H is the half sheet thickness. In this region, an approximate inviscid flow solution can be found which is given by

$$u_r = U_0 \quad (1)$$

$$u_z = -U_0 z/r \quad (2)$$

where U_0 is a constant radial flow velocity and u_r, u_z are the r and z velocity components respectively. U_0 is determined by the exit velocities of the liquid jets, but it is usually assumed to be an input parameter in the analyses. Using this flow solution, an approximate solution for the position of the two liquid-gas interfaces can also be found

$$H = \pm \frac{R_0 H_0}{r} \quad (3)$$

where H_0 is the sheet thickness at the radius R_0 . The constant $R_0 H_0$ is also determined by the geometry of the liquid jets, but is assumed to be an input parameter in the analysis.

Taylor predicted that beyond a critical radius, the sheet is no longer stable and will break-up into droplets. This occurs at a critical Weber number of approximately one. The Weber number based on the thickness of the sheet is

$$We_{sheet} = \frac{U_0^2 H \rho_l}{\sigma} \quad (4)$$

where σ is the surface tension, and ρ_l is the density of the liquid. Using the relation between the half sheet thickness, H , and r an expression for the critical radius of the jet can be determined as

$$R_C = \frac{U_0^2 H_0 R_0 \rho_l}{\sigma} \quad (5)$$

We nondimensionalize the above problem using the radius R_0 , the flow velocity U_0 , and the liquid density. The nondimensional parameters are then ρ_g / ρ_l , $\epsilon = H_0 / R_0$, and $We_0 = \rho_l U_0^2 H_0 / \sigma$ where ρ_g is the gas density. For the analytic solutions to be valid, the parameter ϵ must be a small number. Expression (5) for the critical radius becomes We_0 when nondimensionalized, thus the larger the inlet Weber number, the larger the critical radius. For viscous flows, we have two additional parameters, the inlet liquid Reynolds number, $Re_l = \rho_l U_0 H_0 / \mu_l$, and the liquid to gas viscosity ratio, μ_l / μ_g .

To study this problem, we use the computational domain shown in Figure 2. From here on, all coordinates and parameters are nondimensional. The radius at the inlet is then unity, and the half-sheet thickness at the inlet is ϵ . For all of the results we fix the parameter ϵ to be 0.1. The outlet radius of the domain is 5. An inflow boundary condition is imposed on the left side of the domain with $(u_r, u_z) = (1, -z/r)$. The total stress is set to zero along the right, top, and bottom sides of the domain. A zero curvature condition is imposed for the interfacial boundary condition at the exit, which applies tension in the direction tangent to the interface at the exit. We note that the results are sensitive to the interfacial boundary condition. If the interface is constrained to be horizontal at the exit, no instabilities develop. At the inlet, the sheet location is fixed.

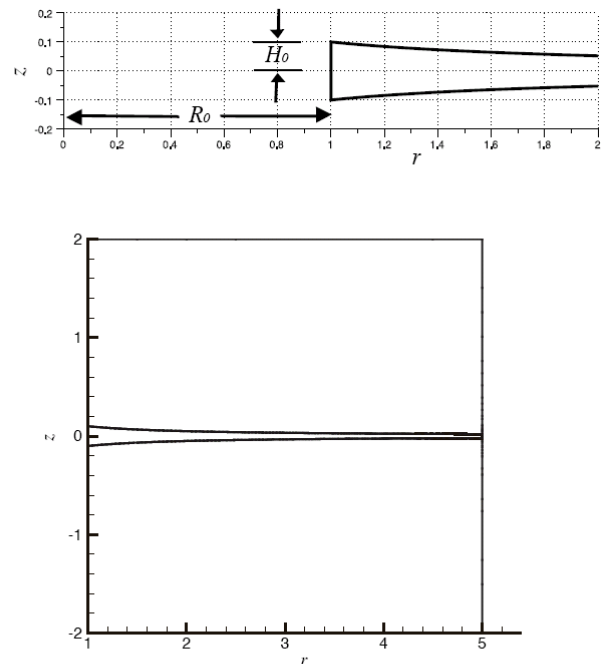


Figure 2. Axisymmetric sheet model with $R_0=1$, $\epsilon = H_0/R_0=0.1$, and a domain length of 5.

Initial conditions for the velocity are given by equations 1 and 2. The initial position for the interface is given by equation 3. The governing equations are the incompressible Navier-Stokes equations and the continuity equation. Interfacial jump conditions are applied along each interface.

Based on the predictions for the critical radius, we expect a stable sheet when We_0 is greater than 5 because the sheet break-up should occur outside of our domain. When We_0 is less than 5, break-up should occur within the domain. To study the stability of the problem, we decrease We_0 in small increments, find steady state solutions for

each value, and record $We_{0,critical}$ where a transition in stability occurs. We will show that the transition in stability manifests itself as either a subcritical or supercritical pitchfork bifurcation with stable branches corresponding to asymmetric stable solutions. If the analytic predictions are correct, the bifurcation will occur at $We_0=5$ which results in having the We based on the sheet half-length equal to one at the exit.

If the sheet position at the inlet is perturbed, stability analysis predicts that two wave packets travel downstream at two different speeds [11]. For $We_{sheet}>1$, the propagating wave speed, V_p , is defined by

$$V_p = \frac{dr_p}{dt} = 1 \pm We_{sheet}^{-1/2} \quad (6)$$

where r_p is the propagating wave location evaluated at a given time, and the time is non-dimensionalized by $t=(U_0/R_0)^{-1}$. In Eq.6, $(1+We_{sheet}^{-1/2})$ corresponds to a fast wave and $(1-We_{sheet}^{-1/2})$ corresponds to a slow wave. When We_{sheet} reaches 1 (the critical radius), this equation predicts that the surface propagation will slow to a halt. We will compare unsteady simulations of a perturbed liquid sheet to the following analytical predictions for $We_0>We_{0,critical}$ and show that the slow wave propagation decreases as We_0 approaches $We_{0,critical}$.

Since the thickness of the sheet decreases in the positive radial direction, it is useful to make the substitution $We_{sheet}=We_0/r_p$ into Eq.6 to get

$$\frac{dr_p}{dt} = 1 \pm \left(\frac{r_p}{We_0} \right)^{1/2} \quad (7)$$

After separating the variables and setting $r_p=1$ at $t=t_0$, the integral of dt/dr_p yields

$$t-t_0 = 2We_0 \left[\pm \frac{1}{\sqrt{We_0}} \left(\sqrt{r_p} - 1 \right) + \ln \left| \frac{1 \pm \frac{1}{\sqrt{We_0}}}}{1 \pm \sqrt{\frac{r_p}{We_0}}} \right| \right] \quad (8)$$

The above equation will be used to validate wave propagation in our unsteady simulations through its comparison to tracked wave edge positions at specified times for a sinusous pulse initiated at the sheet inlet.

3. NUMERICAL METHOD

An hp -finite element method is used to perform the numerical simulations [12]. For the calculations performed in this study we use a basis composed of quartic polynomials on each element ($p = 4$). Quartic polynomials are used because they allow rapid convergence to the exact solution with increasing mesh resolution (5th order spatial accuracy). An unstructured triangular mesh on a rectangular domain is used in all the calculations as shown in Figure 3. The mesh is divided into 3 different regions: the gas layer above the liquid sheet, the liquid sheet itself, and the gas layer below the liquid sheet. Interfacial jump conditions are imposed between the liquid and gas meshes. The mesh is adapted based on the local truncation error in the solution [12]. For unsteady calculations, the time discretization is an A-stable diagonally implicit Runge-Kutta scheme which is 3rd order accurate in time. For the unsteady simulations, we choose a non-dimensional timestep, Δt , of 0.2.

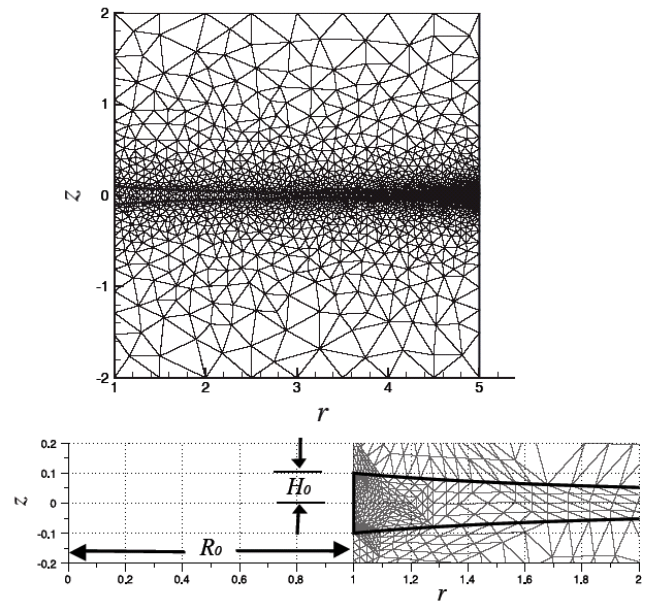


Figure 3. Sheet model using mesh adaptation.

4. SHEET STABILITY

Steady state solutions are found for 36 liquid sheets with the combinations of $\frac{\mu_l}{\mu_g} = 12.5, 25, 50, \frac{\rho_l}{\rho_g} = 32, 160, 800$ and $Re_l = 25, 50, 100, 200$. These values are chosen because they center about the water-air system studied by G.I. Taylor. For all cases, a stable symmetric sheet is found for $We_0=10.0$. The inlet Weber number is then decreased until the sheet becomes asymmetric about the $z=0$ plane and $We_{0,critical}$ is recorded. Since $We_{0,critical}$ is equal to the theoretical critical radius, R_c , it is shown by a vertical dashed line in the following figures. Figure 4 shows the

steady solutions before and after $We_{0,critical}$ for $\frac{\mu_l}{\mu_g}=12.5$, $\frac{\rho_l}{\rho_g}=32$, and $Re_l=50$. In agreement with theoretical results, the sheet is symmetric to the left of the theoretical critical radius and asymmetric to the right. As the inlet Weber number is decreased below $We_{0,critical}$, the location of the asymmetry progresses upstream (Figures 4b, 4c, and 4d).

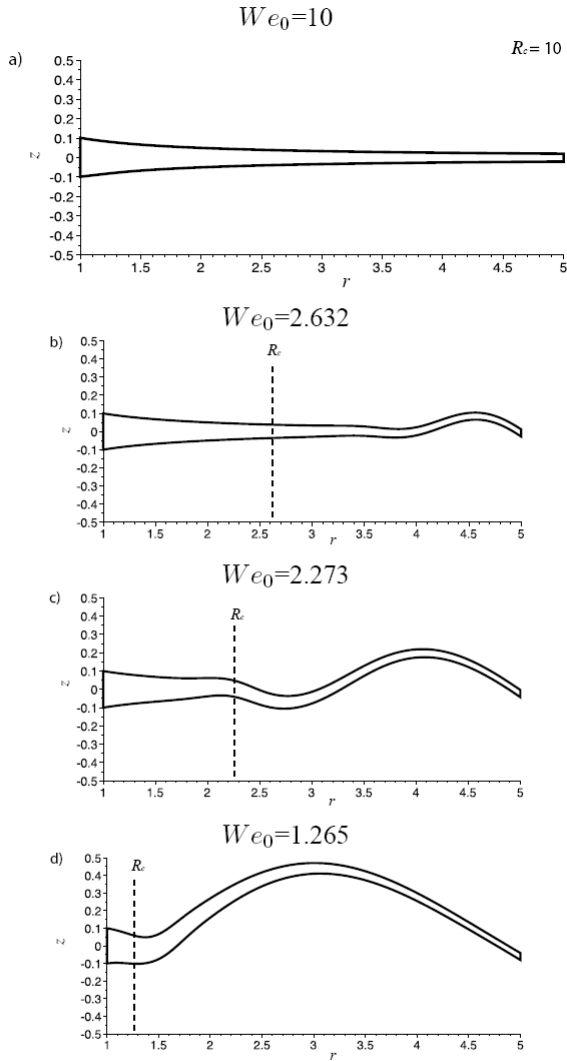


Figure 4. Steady state simulations of a sheet with the properties of $\frac{\mu_l}{\mu_g}=12.5$, $\frac{\rho_l}{\rho_g}=32$, and $Re_l=50$ and each with a decreasing We_0 (top to bottom). To illuminate the asymmetry, the axis is shown here with an aspect ratio of $r:z=5:3$

The direction of the asymmetry in Figure 4 is arbitrary because there are two stable solutions corresponding to mirror images about the z -axis. This leads to the conclusion that there is a pitchfork bifurcation at the stability point. This can occur either supercritically or subcritically. A supercritical bifurcation diagram is shown in Figure 5 with the bifurcation occurring at $We_{0,critical}$. Since We_0 is decreased in our simulation, the amplitude of asymmetry, a ,

vs. We_0 is plotted here and progresses from right to left. The upper and lower stable branches correspond to an upper (Figure 4) and lower mirror image of the asymmetric solution. When we decrease We_0 for the supercritical bifurcation, we travel from right to left on a stable branch and should expect to see the sheet take the same shape for each We_0 as when we increase We_0 and travel from left to right. That is to say, that there is no hysteresis. Also, the the amplitude of asymmetry should slowly evolve from a flat sheet to large scale deformation.

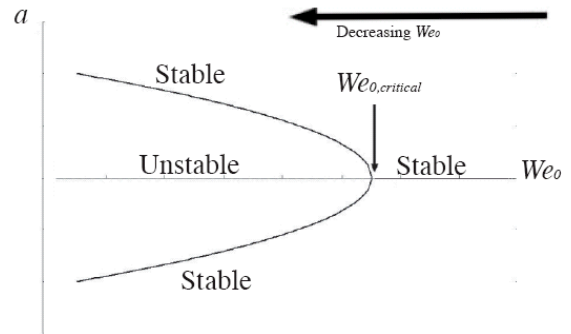


Figure 5. Sketch of a supercritical bifurcation occurring at $We_{0,critical}$. In the simulation, we decrease We_0 to find $We_{0,critical}$ and so the figure should read from right to left.

A subcritical bifurcation diagram is shown in Figure 6. The evolution of the amplitude of asymmetry should not slowly evolve from a flat sheet, but rather a jump will occur because the stable branches do not start at $a=0$ and are separated by unstable branches. The actual bifurcation occurs where the unstable branches meet and the solution is forced to jump to an asymmetric stable branch. After this jump, if we increase We_0 and travel from left to right along the stable branch, we should see asymmetric stable sheet formations, where at the same We_0 before, the sheet was symmetric. In essence, we should see a hysteresis loop as shown in the figure.

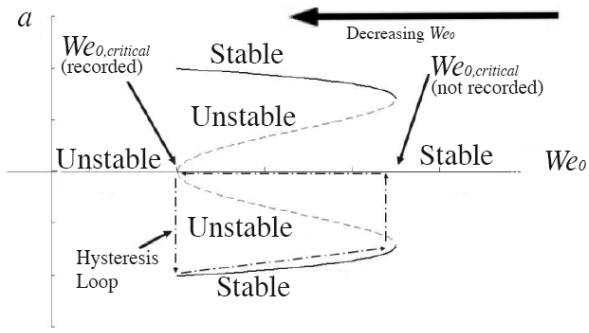


Figure 6. Sketch of a subcritical bifurcation. In the simulation, we decrease We_0 to find $We_{0,critical}$ and so the figure should read from right to left. The $We_{0,critical}$ that is not recorded is a jump to an asymmetric stable solution imposed by mesh adaptation. The $We_{0,critical}$ that is recorded is the bifurcation point where the sheet jumps to an asymmetric stable solution with no mesh adaptation imposed.

To determine the type of bifurcation that occurs, simulations are initiated with We_0 far below $We_{0,critical}$. For these simulations, the sheet is asymmetric because we are beyond the critical point. We_0 is then increased. For the supercritical cases, the bend travels back downstream at the same locations as when We_0 is decreased. If there is no hysteresis, the solution is independent from the direction that we approach it and it is a supercritical bifurcation. This behavior is seen in 9 of the cases studied, which were all combinations of $\frac{\mu_l}{\mu_g}=12.5, 25, 50$, $\frac{\rho_l}{\rho_g}=32$ and $Re_l=25, 50, 100$.

The cases that are subcritical exhibit erratic behavior because the solution can jump between 3 stable solutions. For some cases, the sheet is asymmetric and then symmetric again after reducing the inlet Weber number further. Following the same procedure as for the supercritical case, we find two steady solutions for the same parameters and same inlet Weber number (Figure 7). The difference being that one solution is found by approaching from $We_0 > We_{0,critical}$ and the other is found by approaching from $We_0 < We_{0,critical}$. This hysteresis proves that there are at least 3 stable solutions for this value of We_0 : a pair of asymmetric stable solutions implied by the grid symmetry about the $z=0$ plane, and a symmetric stable solution. For these subcritical cases, it is often difficult to precisely determine $We_{0,critical}$ because the solution can jump branches before reaching $We_{0,critical}$. Mesh adaptation often exacerbates this problem. To try and determine $We_{0,critical}$ as precisely as possible, we turn off mesh adaptation and record the largest We_0 when the solution transitions from symmetric to asymmetric as $We_{0,critical}$.

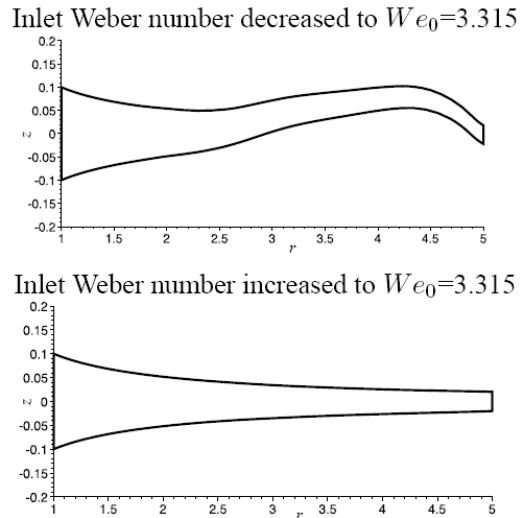


Figure 7. $\frac{\mu_l}{\mu_g}=12.5$, $\frac{\rho_l}{\rho_g}=160$, and $Re_l=50$. To illuminate the asymmetry, the axis is shown here with an aspect ratio of $r:z=5:1$

To study the influence of $\frac{\mu_l}{\mu_g}$, $\frac{\rho_l}{\rho_g}$, and Re_l on $We_{0,critical}$, we plot its contours on a Re_l vs. $\frac{\mu_l}{\mu_g}$ grid (Figures 8, 9, and 10) with each map corresponding to a specific $\frac{\rho_l}{\rho_g}$. Curves of constant Re_g are shown by dotted lines. Nine simulations are represented in each figure. The data points are denoted by O 's where the bifurcation occurs supercritically and by X 's where the bifurcation occurs subcritically. All figures show $We_{0,critical}$ to have a weak dependence on all of the parameters within each chosen range: As $\frac{\mu_l}{\mu_g}$ ranges from 12.5 to 50, Re_l ranges from 25 to 200, and $\frac{\rho_l}{\rho_g}$ quintuples, $We_{0,critical}$ ranges only from 2 to 6.75. This agrees with the expectation that $We_{0,critical}$ should be ≈ 5 ($We_{sheet,critical} \approx 1$). $We_{0,critical}$ has a stronger dependence on liquid Reynolds number than on viscosity ratio, indicating that viscous effects are more important in the liquid phase than in the gas phase, but at higher $\frac{\rho_l}{\rho_g}$, the dependence on $\frac{\mu_l}{\mu_g}$ increases. There is some variation in the plots because it was difficult to precisely determine $We_{0,critical}$ when the bifurcation occurs subcritically.

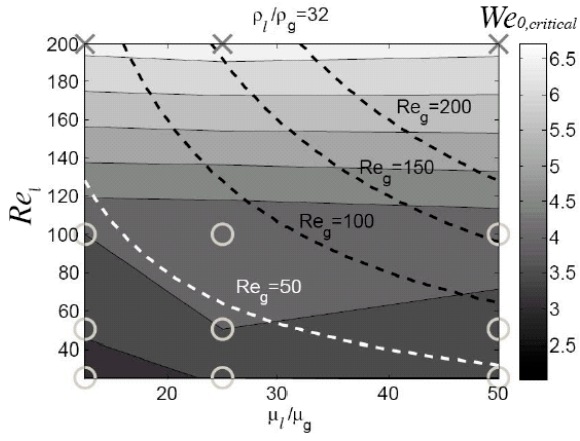


Figure 8. A Re_L vs. $\frac{\mu_l}{\mu_g}$ map with contours of $We_{0,critical}$ and lines of constant Re_g . The actual simulations are represented by O 's where the bifurcation occurs supercritically and by X 's where the bifurcation occurs subcritically.

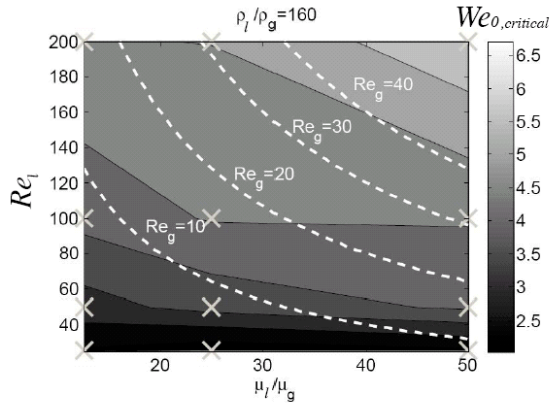


Figure 9. A Re_L vs. $\frac{\mu_l}{\mu_g}$ map with contours of $We_{0,critical}$ and lines of constant Re_g . The actual simulations are represented by O 's where the bifurcation occurs supercritically and by X 's where the bifurcation occurs subcritically.

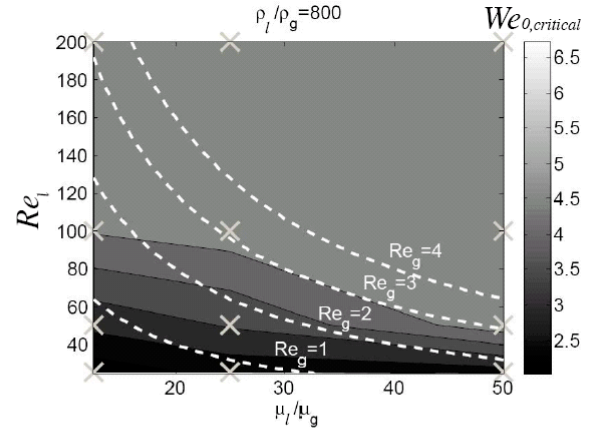


Figure 10. A Re_L vs. $\frac{\mu_l}{\mu_g}$ map with contours of $We_{0,critical}$ and lines of constant Re_g . The actual simulations are represented by O 's where the bifurcation occurs supercritically and by X 's where the bifurcation occurs subcritically.

5. PERTURBATION RESPONSE

When an antisymmetric (sinuous) pulse is introduced, we expect it to propagate at a speed determined by Eq. 6. We perform unsteady simulations to verify these predictions. A sinuous pulse is initiated by moving the inlet nodes, located at $(r_{inlet}, z_{inlet}) = (1, \varepsilon)$ and $(1, -\varepsilon)$, using the equation below.

$$z_{inlet} = \varepsilon + \left[1 - \cos\left(\frac{2\pi(t - t_0)}{T}\right) \right] \quad (9)$$

A is the amplitude of the wave, t_0 is the time when the wave is initiated, and the inlet perturbation stops after a time of T . We perturb the sheets with $A=0.01$, $t_0=0.2$, and $T=2.0$. A fast moving wave and a slow moving wave is produced as a result of the perturbation, as shown in Figure 12. To track the position of each wave as a function of time, we follow the trailing edge of the fast moving wave and the leading edge of the slow moving wave. This is done by tracking the intersection made by the interface with the mean position of the sheet.

We present two cases for our unsteady results. The case of $\frac{\mu_l}{\mu_g}=12.5$, $\frac{\rho_l}{\rho_g}=32$, $Re_l=50$ is supercritical. For this case, the asymmetry occurring at $We_{0,critical}$ manifests itself as a small bend much like that seen in Figure 4. The case of $\frac{\mu_l}{\mu_g}=12.5$, $\frac{\rho_l}{\rho_g}=800$, $Re_l=25$ is subcritical. For this case, the asymmetry occurring at $We_{0,critical}$ is a large

amplitude deformation. We run both cases with various values of We_0 's that are close to $We_{0,critical}$. For the supercritical case (Figure 13), a plot of r_p versus t for 4 sheets is shown: 2 sheets with $We_0 > We_{0,critical}$, 1 sheet with $We_0 = We_{0,critical}$, and 1 sheet with $We_0 < We_{0,critical}$. For the subcritical case (Figure 14), the same plot is shown for two sheets of $We_0 > We_{0,critical}$. The tracked wave position is shown by '+'s and Eq. 8 is shown by the solid curves.

For the supercritical case, $We_{0,critical}$ is 3.57. Figure 13 shows a plot of the fast and slow waves for $We_0 = 2.875, 3.571, 5,$ and 10 . The slope, V_p , is nearly independent of position for all fast waves. When We_0 is 10 and 5, the slow wave speed is also almost independent of position. For $We_0 < We_{0,critical}$, the slow wave decelerates as it nears the sheet edge. This agrees with the prediction that a propagating disturbance will slow to a stop at the sheet's critical radius. For the case of $We_0 = 2.875$, the sheet is unstable, and the slow wave merges with the developing asymmetry. Although the wave does not completely stop in the slow case, the wave propagation matches reasonably with stability theory for both the slow and fast wave.

For the subcritical case, $We_{0,critical}$ is 2.22 and we present sheets with $We_0 = 5$ and 10 . Figure 14 matches well with stability theory for the fast wave and is qualitatively correct for the slow wave. V_p follows Eq.6 and is nearly independent of position for both the slow and fast wave for large We_{sheet} . The reverse wave that is shown in Figure 14 for $We_0 = 5$ is actually an asymmetry evolving to its steady state formation, because the perturbation causes the solution to jump to an asymmetric stable branch. Figure 15 shows the wave evolution for the supercritical case. The sheet asymmetry caused by the stability change begins to evolve after only 5.4 non-dimensional time units and stops after 83.2 non-dimensional time units.

5. CONCLUSION

Different behaviors arise when a liquid sheet reaches its critical radius. A change of stability manifests itself as sheet asymmetry and the solution bifurcates either supercritically or subcritically depending on the chosen density ratio, viscosity ratio, and Reynolds number. The location of the critical radius where the stability change occurs has a weak dependence on these parameters and happens near $We_{sheet} = 1$ as predicted by G.I. Taylor. A sinusoidal pulse at the sheet inlet produces a fast and slow moving wave which propagate downstream at speeds predicted by stability analysis.

5. REFERENCES

1. F. Savart. *Ann. Chim. Phys.*, LIX:266, 1833.
2. W.N. Bond. *Proc. phys. Soc. XLVII*, 549, 1935.
3. G.I. Taylor. *Proceedings of the Royal Society of London A*, CCLIII:289–95,313–321, 1959.
4. J.C.P. Huang. *Journal of Fluid Mechanics*, 43(2), 1970.
5. G.I. Taylor. *Proceedings of the Royal Society*, CCLIX:1–17, 1960.
6. Y.H. Jung C.H. Lee and S.H. Chung. *Atomization and Sprays*, 9, 1999.
7. Y.J. Choo and B.S. Kang. *Experiments in Fluids*, 34, 2004.
8. John W.M. Bush and Alexander E. Hasha. *Journal of Fluid Mechanics*, 511, 2004.
9. Erik McWilliams Erik Miller, Beau Gibson and Jonathan P. Rothstein. *Applied Physics Letters*, 87, 2005.
10. S.P.Lin and W. Y. Jang. *Physics of Fluids*, 15(6), 2003.
11. S.P.Lin. *Breakup of Liquid Sheets and Jets*. Cambridge University press, 2003.
12. B.T. Helenbrook. *Comp. Meth. Appl. Mech. Eng.*, 191(273-294), 2001. *

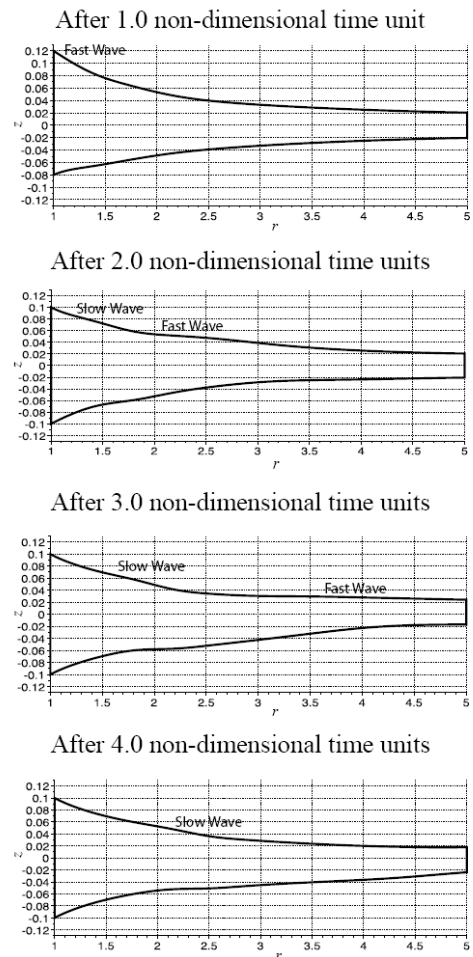


Figure 12. By perturbing the inlet nodes in the positive z direction, 2 waves are produced. The first wave propagates much faster than the second wave. To illuminate the wave propagation, the axis is shown here with an aspect ratio of $r:z=25:4$

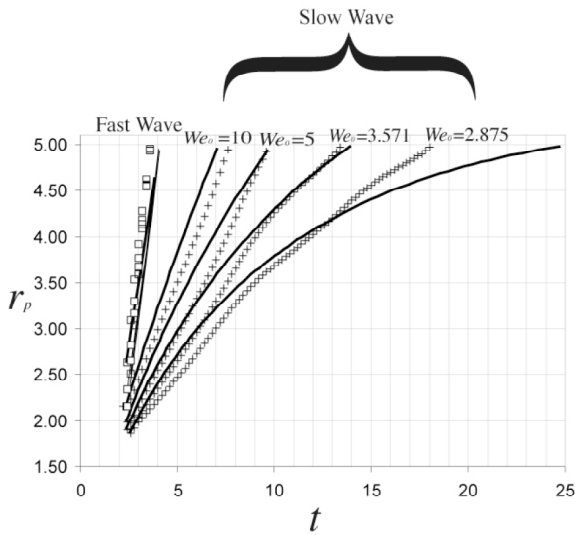


Figure 13. Wave position vs. time for the case where $\frac{\mu_l}{\mu_g}=12.5$, $\frac{\rho_l}{\rho_g}=32$, and $Re_l=50$. The '+'s represent the numerically tracked wave positions and the solid curves represent the exact solution to the stability analysis. $We_{0,critical}=3.571$

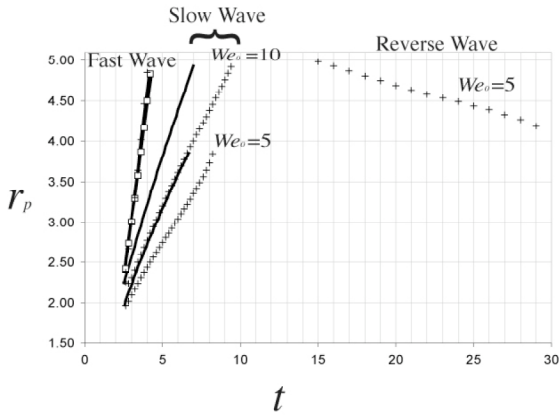


Figure 14. Wave position vs. time for the case where $\frac{\mu_l}{\mu_g}=12.5$, $\frac{\rho_l}{\rho_g}=800$, and $Re_l=25$. The '+'s represent the numerically tracked wave positions and the solid curves represent the exact solution to the stability analysis. $We_{0,critical}=2.22$

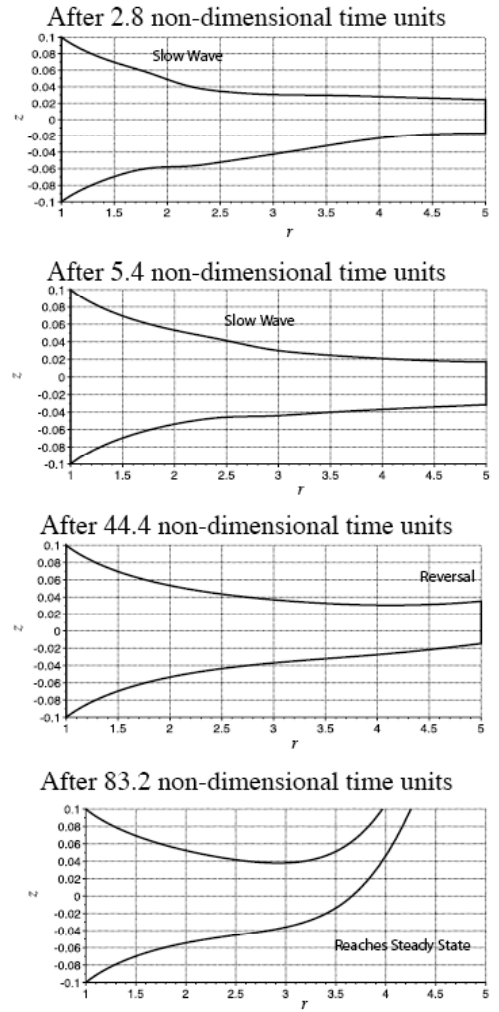


Figure 15. $\frac{\mu_l}{\mu_g}=12.5$, $\frac{\rho_l}{\rho_g}=800$, $Re_l=25$, and $We_0=5.0$. The slow wave propagates downstream. Much later, a slight asymmetry evolves into the steady state solution. To illuminate the wave propagation, the axis is shown here with an aspect ratio of $r:z=25:3$